

Pyrolysis Pathways of Sulfonated Polyethylene, an Alternative Carbon Fiber Precursor

Jarod M. Younker,^{*,†} Tomonori Saito,[‡] Marcus A. Hunt,[‡] Amit K. Naskar,[‡] and Ariana Beste[§]

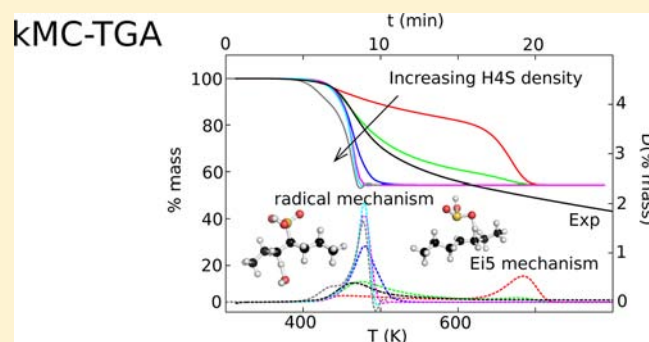
[†]Oak Ridge Associated Universities, 1 Bethel Valley Road, Oak Ridge, Tennessee 37831-6164, United States

[‡]Materials Science and Technology Division, Oak Ridge National Laboratory, 1 Bethel Valley Road, Oak Ridge, Tennessee 37831-6053, United States

[§]Joint Institute for Computational Sciences, University of Tennessee, 1 Bethel Valley Road, Oak Ridge, Tennessee 37831-6164, United States

S Supporting Information

ABSTRACT: Polyethylene is an emerging precursor material for the production of carbon fibers. Its sulfonated derivative yields ordered carbon when pyrolyzed under inert atmosphere. Here, we investigate its pyrolysis pathways by selecting *n*-heptane-4-sulfonic acid (H4S) as a model compound. Density functional theory and transition state theory were used to determine the rate constants of pyrolysis for H4S from 300 to 1000 K. Multiple reaction channels from two different mechanisms were explored: (1) internal five-centered elimination (E_iS) and (2) radical chain reaction. The pyrolysis of H4S was simulated with kinetic Monte Carlo (kMC) to obtain thermogravimetric (TGA) plots that compared favorably to experiment. We observed that at temperatures <550 K, the radical mechanism was dominant and yielded the *trans*-alkene, whereas *cis*-alkene was formed at higher temperatures from the internal elimination. The maximum rates of % mass loss became independent of initial OH radical concentration at 440–480 K. Experimentally, the maximum % mass loss occurred from 440 to 460 K (heating rate dependent). Activation energies derived from the kMC-simulated TGAs of H4S (26–29 kcal/mol) agreed with experiment for sulfonated polyethylene (~ 31 kcal/mol). The simulations revealed that in this region, decomposition of radical HOSO_2 became competitive to α -H abstraction by HOSO_2 , making OH the carrying radical for the reaction chain. The maximum rate of % mass loss for internal elimination was observed at temperatures >600 K. Low-scale carbonization utilizes temperatures <620 K; thus, internal elimination will not be competitive. E_iS elimination has been studied for sulfoxides and sulfones, but this represents the first study of internal elimination in sulfonic acids.



INTRODUCTION

Carbon fiber and its composites are of growing importance in the construction of materials that balance the need to be lightweight and strong.¹ These fibers have high tensile strengths of up to 7 GPa and densities of 1.75–2.00 g mL⁻¹.^{1,2} They are also resistant to chemical attack, making them extremely durable. The greatest impediment to wider implementation of carbon fibers into consumer products is the high price of precursors. Polyacrylonitrile (PAN) is the preeminent precursor in the market.^{1–3} Cost analysis revealed that one-half the cost of carbon fiber was derived from the manufacture of PAN.⁴ The discovery of a cheaper precursor would greatly diminish the cost of carbon fiber and open other markets to its use. Oak Ridge National Laboratory (ORNL) and its partners in the Automotive Composites Consortium (ACC) have been exploring alternative means of producing carbon fiber that would be cost-effective in the construction of automobiles.

One attractive alternative precursor, polyethylene (PE), is an inexpensive, petrochemical-derived, melt-processable polymer. PE is omnipresent in our society, having penetrated nearly

every plastic market.⁵ Another advantage of PE over PAN is its favorable process economy due to melt spinnability. Unfortunately, carbonization of PE does not produce carbon residue or char; the heated PE is instead lost as short-chain hydrocarbons.^{6–8} In 1990, Postema et al. showed that, upon heating, the sulfonated derivative of linear low-density polyethylene (LLDPE) produces an amorphous charred mass.⁶ Recently, Hunt et al. have refined this method by spinning and then sulfonating a bicomponent extrusion of PE and polyactic acid to create patterned, continuous carbon fiber.⁹

Sulfonation is achieved by pulling PE fibers through a solution of “fuming” sulfuric acid at 70 °C.^{6,9–13} Following sulfonation, a small percentage of carbon in the PE hydrocarbon is found sulfonated in the resulting polymer. After an equilibrium sulfonation, if an even distribution is assumed, one out of every five to seven carbons is substituted, with $\sim 70\%$ of the substitutions being sulfonic acid (various sulfones and

Received: December 13, 2012

Published: April 5, 2013

sulfates groups comprise the remaining sulfur-containing moieties).^{9,12} We, therefore, chose *n*-heptane-4-sulfonic acid (H4S) as a model compound for sulfonated PE for this study. This model guaranteed that all reactions occurred at a secondary carbon and that the alkane backbone was acyclic (see Figure 1). The first step in the carbonization of sulfonated

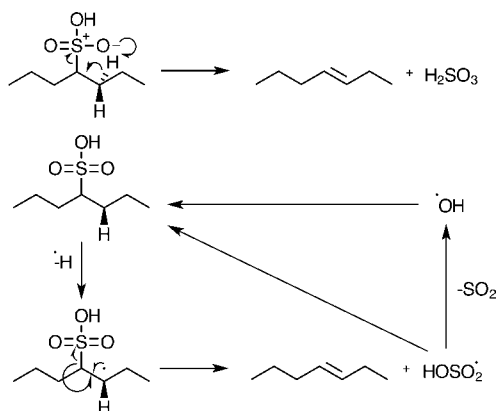


Figure 1. Scheme showing E_iS elimination (top) and the radical chain reaction (bottom) for H4S.

PE is elimination of sulfur, oxygen, and hydrogen via pyrolysis to yield the unsaturated polyolefin. We studied two probable elimination mechanisms: five-centered internal elimination (E_iS) and a radical chain reaction, as schematically shown in Figure 1.

E_iS elimination is analogous to five-centered elimination in amine oxides (Cope elimination).¹⁴ Such a mechanism is termed E_i in sulfoxide/sulfone chemistry,^{14–20} being more facile for sulfoxides than sulfones.^{20,21} Although the traditional structural representation of the E_iS reaction, as displayed in Figure 1, involves $S=O$, in the schematic we have shown an ylide structure as there exists no π bond between S and O in the sulfonic acid group. To our knowledge, the internal elimination mechanism for sulfonated alkane derivatives has not been studied.

The second mechanism studied involved two interconnected radical chain reactions. In particular, we investigated chain propagation through the $\dot{O}H$ and $HOS\dot{O}_2$ radicals. Because the experimental setup does not include a source of continuous radical formation, the only viable route of product formation through a radical mechanism is radical chain formation. Experimentally, the heating of poly(vinyl)sulfonic acid produces a carbonized material (vide infra).⁹ The amount of carbon char is correlated with the degree of sulfonation. Therefore, radical mechanisms were selected that yielded both a long-chain alkene and a reaction chain. The only path that leads to such a chain, as well as the experimentally observed olefin, involves α -H abstraction followed by liberation of hydroxysulfonyl radical ($HOS\dot{O}_2$, which can undergo further decomposition to $\dot{O}H$ and SO_2).

One can argue that the preferable site of hydrogen abstraction is the sulfonated carbon. Although the resulting radical would be stabilized through delocalization, β -scission of the carbon chain would follow, as demonstrated in cerium-coordinated α -H abstraction from the SCH_3 group of $ROSO_2CH_3$.²² Termination of radicals by chain scission of the alkane would increase formation of small olefinic molecules, reducing char yield. Mass spectrometry of evolved gases during

pyrolysis of the sulfonated polyethylene fiber shows SO_2 and H_2O as major products. Alternatively, hydrogen transfer from an adjacent carbon is possible. This returns us to the proposed mechanism. As such, we will not consider abstraction at the sulfonated carbon site, or for that matter, abstraction at an end methyl group or at a site that would terminate the radical reaction chain. The agreement between our results with experiment validates this assumption.

There are multiple possibilities for radical chain initiation. One possible way to initiate the reaction is through homolytic cleavage of the $HOS\dot{O}_2$ from H4S, which can then react by abstracting a nearby hydrogen. Second, decomposition of $HOS\dot{O}_2$ radical yields $\dot{O}H$ as the chain carrying radical. Third, a small amount of residual $\dot{O}H$ radical, likely present in the polymer following sulfonation, initiates the reaction. The possibility of homolytic cleavage of H4S to yield \dot{H} from sulfonic acid group containing carbon (with a resonance stabilized counter radical) could be another catalytic driver for the cleavage of the $HOS\dot{O}_2$ from H4S, which can yield H_2SO_3 after combination with \dot{H} , or generates $\dot{O}H$ and SO_2 after subsequent decomposition.

In all cases, following the first cycle of reactions, $\dot{O}H$ or $HOS\dot{O}_2$ abstracts hydrogen at the H4S α -site. Following α -H abstraction, $HOS\dot{O}_2$ dissociates homolytically, yielding hept-3-ene. $HOS\dot{O}_2$ may then decompose into SO_2 gas and $\dot{O}H$, making $\dot{O}H$ the chain carrying radical, or $HOS\dot{O}_2$ may perform the next α -H abstraction to give H_2SO_3 . The products formed following the first cycle of reactions would be $HOS\dot{O}_2$, SO_2 , $\dot{O}H$, and the alkene.

To understand the desulfonation step for sulfonated PE, the pyrolysis of H4S was investigated with density functional theory (DFT). Conventional transition state theory (TST) was then used to calculate rate constants for the two competitive mechanisms: E_iS and radical chain mechanism. Using the computed rate constants, we simulated the pyrolysis of H4S with kinetic Monte Carlo (kMC). kMC results were compared to the experimental characterization of sulfonated PE by thermogravimetric analysis (TGA). We assumed infinite chain length in the kMC simulations.

EXPERIMENTAL DETAILS

PE fibers were pulled through a bath filled with oleum maintained at 70 °C. To achieve a quantitative sulfonation, the soak time was set at 60 min. In TGA, a substance is weighed on a balance while being heated at a constant rate (°C/min).²³ The result is a measure of the % mass loss of the sample versus time or temperature. When heated, sulfonated PE undergoes a mass loss at 150–200 °C, and we defined it as the desulfonation reaction. The desulfonation reaction was monitored with TGA at a heating rate of 2.5, 5, 10, and 20 °C/min. All samples were predried at 100 °C for 1 h in situ before starting the TGA scan. The degree of sulfonation (DS) of the quantitatively sulfonated PE fibers was 0.4 (mol (sulfonic acid)/mol (PE)).⁹ DS was determined as a molar ratio of sulfonic acid to polyethylene using the weight loss up to 400 °C from TGA as a weight fraction of the sulfonic acid, where all of the functional groups on PE were assumed as sulfonic acid.

Activation energies were determined by the method of Flynn and Wall:²⁴

$$E_a = \frac{-R}{b} \left(\frac{d \log \beta}{d(1/T)} \right) \quad (1)$$

where E_a is the activation energy, R is the gas constant, $b = 0.457$, and the value in the parentheses is the slope of the log of the heating rate ($\beta = 2.5\text{--}20$ °C/min) versus $1/T$, where T is chosen to correspond to

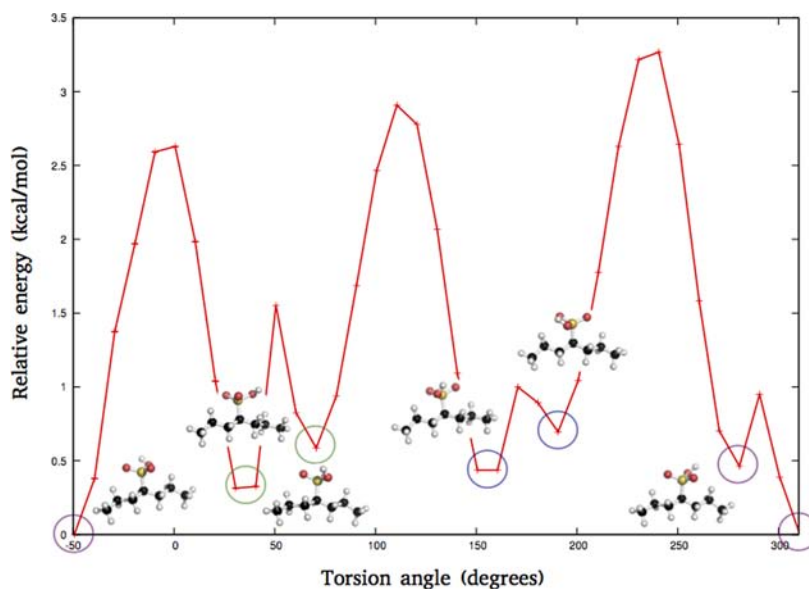


Figure 2. Binned minima from R-SO₃H rotational coordinate. Reactant [A] is in purple, [B] is in green, and [C] is in blue.

the temperature at which a constant percent weight loss of the sample is achieved (0.5%, 1.0%, 2.5%, 5.0%, 7.5%, 10.0%, 12.5%, 15.0%, 17.5%, and 20.0% loss).

COMPUTATIONAL DETAILS

All electronic structure calculations were carried out with the NWChem program package (6.0) utilizing the M06-2X functional.^{25–27} This hybrid meta-functional was developed to improve the description of medium range correlation and has performed well for sulfur-containing molecules.^{19,28–31} We are mindful of possible errors introduced by the quadrature grid size when employing M06-2X and have utilized the number of integration points recommended by Wheeler and Houk.³²

In this work, geometries were optimized at M06-2X/6-31G**. Reactants, precomplexes, transition states, intermediates, postcomplexes, and products were confirmed by frequency analysis. We included diffuse and polarization functions on the hydrogens, which are directly involved in the transition states. Even though we used tight convergence criteria (see the Supporting Information for details) for the stationary-point searches, small imaginary frequencies (<60 cm⁻¹) were present in many of the molecules. These artifacts can be traced to instabilities in the numerical derivatives used to calculate the mass-weighted Hessian. Displacements along the imaginary normal modes showed that the geometry was either a minimum or a transition state (see the Supporting Information for displacement energies).

For the BDEs, thermal corrections included translational, rotational, and vibrational contributions; for the latter, the harmonic approximation was applied. Energies at stationary points were computed with the 6-311++G(3df,3pd) basis set, and 0 K energy differences were zero-point corrected. The corrected energies were converted into enthalpies, and the BDE was obtained as the difference of the sum of the thermally corrected enthalpy of the products and the thermally corrected enthalpy of the reactant.

For any one step in the pyrolysis mechanisms, multiple reactant conformers were explored. We refer to the reaction profile for any one conformer as a reaction channel. To find each unique reaction channel, the transition state was first identified. We then followed the imaginary mode to the reactant or product by optimizing the geometry obtained by displacement along the imaginary mode. For bimolecular reactions, a pre- or postcomplex was formed that is at a lower energy than the infinitely separated reactants or products.

To determine the number of conformers needed to study H4S, we searched the R-SO₃H rotation coordinate and found six unique minima (see Figure 2). These six minima can be reduced to three

reactants (termed [A], [B], and [C]) separated by rotational barriers of ~3 kcal/mol. We rationalize this reduction in the number of reactants by noting the following two observations. One, the two minima that compose each reactant were separated by rotational barriers of <1 kcal/mol. A thermodynamic distribution between the two minima would result. Two, the difference in R-SO₃H angles between the two minima was <20°, where each minima corresponded to a 180° torsional rotation along the R-S-O-H bond. Given this observation, we assume that the corresponding transition states have a similar energetic offset. We therefore assumed three reactant conformers resulting from rotation of the sulfonic acid substituent. In the case of the E₁S mechanism, there were, in addition to the three reactants of the sulfonic acid, two unique α-H's, for a total of six conformers. In the case of the radical mechanism, four α-H's were available for abstraction by OH, giving a total of 12 unique conformers. Each of the three oxygens of HOSO₂ can abstract any of the four α-H's yielding a total of 36 distinct conformers for α-H abstraction by HOSO₂. There were 12 conformers of the radical alkane intermediate that reacted to yield hept-3-ene and HOSO₂.

Rate constants for elementary reactions were calculated with our Python code, which is interfaced to the NWChem program package.²⁵ We applied TST and included a Wigner tunneling correction (κ) to compute unimolecular rate constants:^{33–35}

$$k(t) = \kappa(T) \frac{k_B T}{h} \frac{Q_{TS}(T)}{Q_A(T)} e^{-\Delta E/RT} \quad (2)$$

where k_B is the Boltzmann constant, R is the ideal gas constant, T is the temperature, h is the Planck constant, ΔE is the zero-point corrected activation barrier, and Q are the partition functions for the transition state (TS) and reactant or precomplex (A). Anharmonic effects were incorporated for low frequency vibrations up to 110 cm⁻¹, which corresponded to 1–15 modes. Within the independent mode approximation, the anharmonic potentials were obtained by displacement along normal modes, and 9 energy points per mode were used for a fourth-order polynomial fit. The anharmonic vibrational partition functions were computed with the semiclassical Wigner–Kirkwood approximation, as outlined in Beste et al.³⁵ Rate constants were recorded every 10 °C from 300 to 1000 K.

The cumulative second-order rate constants were calculated assuming thermodynamic control: $k_i' = k_i K_{eq}$, where the unimolecular rate constant k_i was determined as described above with K_{eq} being the equilibrium constant.

Arrhenius plots of the cumulative second-order rate constants ($\ln k_i'$ versus $1/T$) were nonlinear. Therefore, we fit the constants to the equation proposed by Kooij:³⁶

$$k_i' = BT^\alpha e^{-E_0/RT} \quad (3)$$

where B , α , and E_0 are temperature-independent parameters. Parameters were fit nonlinearly to the expression:

$$\ln k_i' = \ln B + \ln((1/x)^\alpha) - E_0x/R \quad (4)$$

where $x = 1/T$. When two temperature ranges were necessary for an adequate fit, starting values were derived from a nonlinear fit over the entire temperature range.

The pyrolysis of H4S was simulated using kinetic Monte Carlo (kMC) as implemented in the SPPARKS package developed at Sandia National Laboratory using the rate constants derived from DFT and TST.³⁷ The initial molecule count for H4S was 3×10^7 . The initial radical to molecule count ratio ($\dot{O}H/H4S$) varied from 3.3×10^{-8} to 6.7×10^{-3} . TGA plots from 300 to 800 K, at heating rates of 2.5, 5, 10, and 20 °C/min, were obtained by allowing the simulation to proceed for a set time at a given temperature. The final molecule counts were then used as input for the following incremental temperature, together with the rate constants at that temperature, and the simulation was advanced. In determining remaining mass, SO_2 and H_2O were considered lost. The same Flynn and Wall procedure detailed above was followed to obtain the activation energies from the kMC simulations where a cubic spline was used to interpolate between recorded data points using the statistical package R.³⁸ The volume of the simulation cell was set to obtain densities of 1.6 pg mL⁻¹, 16 pg mL⁻¹, 160 pg mL⁻¹, 1.6 ng mL⁻¹, 16 ng mL⁻¹, 160 ng mL⁻¹, and 1.6 μg mL⁻¹, approaching the experimental density of sulfonated PE (1.6 g mL⁻¹). Pyrolysis simulations of H4S with kMC at the experimental density were unsuccessful due to numerical issues when the number of molecules was increased beyond 10^8 and for volumes less than 10^{-11} L. To run the simulations at a density of 160 ng mL⁻¹, we therefore increased the number of H4S molecules to 3×10^8 .

RESULTS AND DISCUSSION

Degree of Sulfonation and Carbon Yield. The degree of sulfonation and carbon yield were readily determined by analyzing a piece of the sulfonated polyethylene fiber using TGA. TGA curves of representative partially sulfonated PE fiber and completely sulfonated PE fiber are found in Figure 3. Initial weight loss (derivative peak range 160–175 °C) corresponds to the loss of functional groups on PE fiber, and the second weight loss (derivative peak range 450–480 °C) corresponds to degradation of unreacted PE, which was confirmed with TGA of neat or nonsulfonated PE. If the degradation of PE around 450–480 °C was not observed in TGA (Figure 3B), the functionalized fiber was fully stabilized. The weight loss until 400 °C was assigned as a weight fraction of functional groups and used to calculate the degree of sulfonation. As shown in Figure 3A, the representative partially sulfonated polyethylene gives 25% charred residue; on the other hand, the completely sulfonated polyethylene yields ~40% charred residue. Partially functionalized PE fiber correlates well with diffusion of the reactant, which has been confirmed by the resulting hollow carbon fibers.⁹ When fully functionalized PE fibers are carbonized, the possibility of formation of hollow carbon fibers was eliminated. Thus, we conclude extensively sulfonated polyolefins yield alkene derivatives, which enhance char formation under inert atmosphere. A gas chromatograph coupled with mass spectrometry of evolved gases during pyrolysis (in TGA instrument) of a completely sulfonated polyethylene fiber that yields carbon shows the presence of SO_2 and H_2O as major pyrolysis products. The ordered carbon structure from the skin

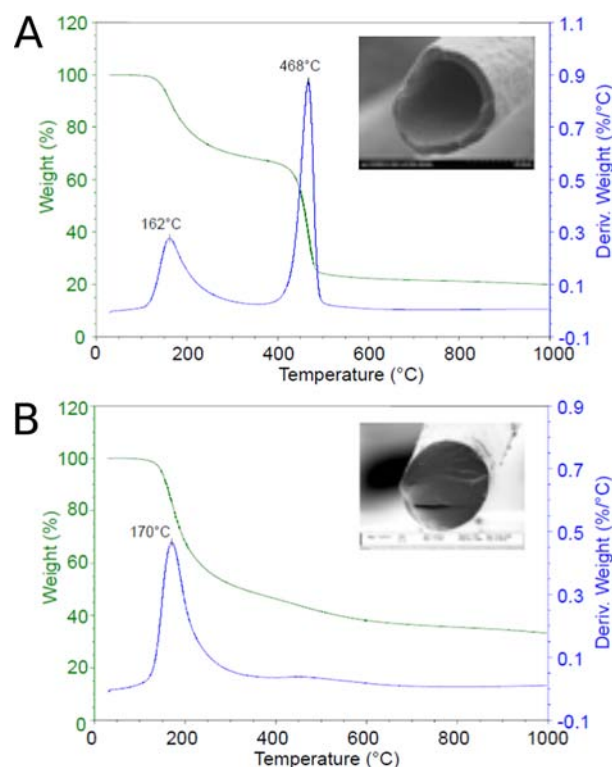


Figure 3. (A) TGA thermogram of partially functionalized PE fiber (inset: scanning electron micrograph of pyrolyzed fiber from a partially sulfonated polyethylene). (B) TGA thermogram of fully functionalized PE fiber (inset: scanning electron micrograph of pyrolyzed fiber from a fully sulfonated polyethylene).

of a fully sulfonated precursor, as observed under a transmission electron microscope, is shown in Supporting Information Figure S1. These results limit the number of possible reactions of interest to those that lead to the formation of olefin.

Geometry and Bond Dissociation Energies of Sulfonic Acid Derivatives. To test the lability of the sulfonic acid, we have determined several BDEs at M06-2X/6-311++G-(3df,3pd)//M06-2X/6-31G** as shown in Figure 4. RSO_2-OH and $R-SO_3H$ BDE values for H4S were 89.8 and 76.8 kcal/mol, respectively. They compared favorably to the experimental BDEs of methanesulfonic acid: $HO-SO_2CH_3 =$

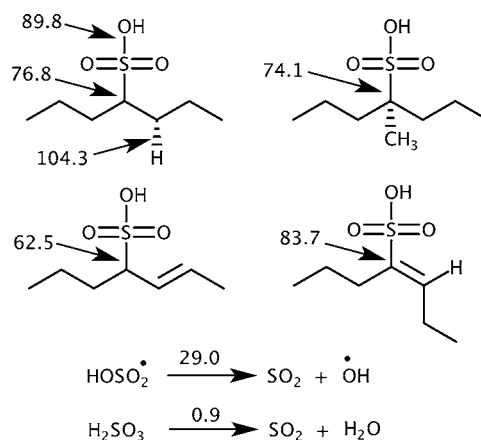


Figure 4. M06-2X/6-311++G(3df,3pd)//M06-2X/6-31G** BDEs in kcal/mol at 298 K.

86.6 ± 3 kcal/mol and HOSO₂-CH₃ = 77.5 ± 3 kcal/mol.³⁹ In low density poly(vinyl)chloride polymers, it is believed that dehydrochlorination begins at a tertiary carbon, with subsequent polymer unzipping aided catalytically by liberated HCl gas.^{40,41} Evidence that initiation began at a tertiary site was also found in sulfoxide polymers.⁴² The R-SO₂OH BDE from *n*-4-methylheptane-4-sulfonic acid (sulfonation at a tertiary carbon) was calculated to be 2.7 kcal/mol lower than the BDE at H4S (sulfonation at a secondary carbon). Because double bonds are formed during the course of the reaction, we also determined the BDEs for hept-2-ene-4-sulfonic acid and hept-3-ene-4-sulfonic acid. In contrast to hept-3-ene-4-sulfonic acid, resonance delocalization aided in sulfonic acid dissociation for hept-2-ene-4-sulfonic acid (BDE = 62.5 kcal/mol). Overall, these large values would indicate that the contribution of the dissociation of HOSO₂ from H4S to pyrolysis is small. Although homolytic cleavage is unfavorable, only a small amount of dissociated HOSO₂ (with or without subsequent decomposition to SO₂ and OH) is needed for catalysis.

A range of energies, 25–30 kcal/mol, has been calculated for the decomposition of HOSO₂.^{43–46} Experimentally, the value is 30.5 kcal/mol,⁴⁷ although a more recent value of 27.1 kcal/mol has been reported.⁴⁸ Our value of 29 kcal/mol compared well to literature. Our reported BDE for H₂SO₃ decomposition (0.9 kcal/mol) is in line with the unstable nature of the species, with it being isolatable only within the gas phase, as well as other computational work.^{49–52}

Reaction Channels. The two pyrolysis mechanisms studied in this work are detailed below and displayed graphically in Figure 1. For bimolecular reactions, the precomplex is the associated minimum-energy adduct prior to decomposition, while reactants are defined as being at infinite distance. The postcomplex is the associated minimum-energy adduct following decomposition, while products are defined as being at infinite distance.

Internal Elimination. Internal five-centered or Cope-like elimination is a concerted process. Alternatively, the reaction can be viewed as that of a ylide. This elimination is shown in Figure 1. During H4S conversion to the olefin via E₅ elimination, sulfurous acid (H₂SO₃) was liberated. Although isolatable in the gas phase, in solution, H₂SO₃ is a nonisolatable transient species, which quickly decomposes into SO₂ and H₂O.^{49–52} Water can then catalyze the decomposition.⁵⁰

- (1) H₂SO₃ → SO₂ + H₂O (H₂SO₃ decomposition)
- (2) H₂SO₃ + H₂O → SO₂ + 2H₂O (H₂O-catalyzed H₂SO₃ decomposition)

A four-centered internal elimination (E₄) is also conceivable, being prevalent in ethers and halogenated alkanes.¹⁴ However, despite an exhaustive search, we did not locate a corresponding E₄ transition state for H4S. The formation of a four-centered transition state (C-S-H-C) was sterically hindered by one of the three oxygens of the SO₃H group.

Radical Chain Reaction. In the radical chain mechanism, OH or HOSO₂ abstracts an α-H from H4S (see Figure 1). To have a viable radical chain, the resulting radical alkane intermediate decomposes to olefin and HOSO₂. HOSO₂ follows two paths: (1) decomposition to SO₂ and OH or (2) HOSO₂ continues as the radical responsible for the chain propagation, abstracting the next α-H. If the second pathway is followed, the resulting H₂SO₃ then decomposes as detailed for the internal elimination. The resulting kMC-simulated TGAs for the reactions with trace initial amounts of OH and HOSO₂ are

identical. This result will be explored later in the text. Unimolecular and H₂O-catalyzed decomposition of HOSO₂ were considered:

- (1) HOSO₂ → SO₂ + OH (HOSO₂ decomposition)
- (2) HOSO₂ + H₂O → SO₂ + H₂O + OH (H₂O-catalyzed HOSO₂ decomposition)

Five-Membered Internal Elimination (E₅). As discussed in Computational Details and as shown in Figure 2, we have assigned H4S to three conformers: [A], [B], and [C]. For E₅ there were two unique α-H's, one on either side of the sulfonic acid substituent, involved in this pathway. Therefore, unimolecular elimination proceeded via six reaction channels. The reaction barriers for elimination in four of the channels were ~50 kcal/mol (see Figure 5). In the remaining two

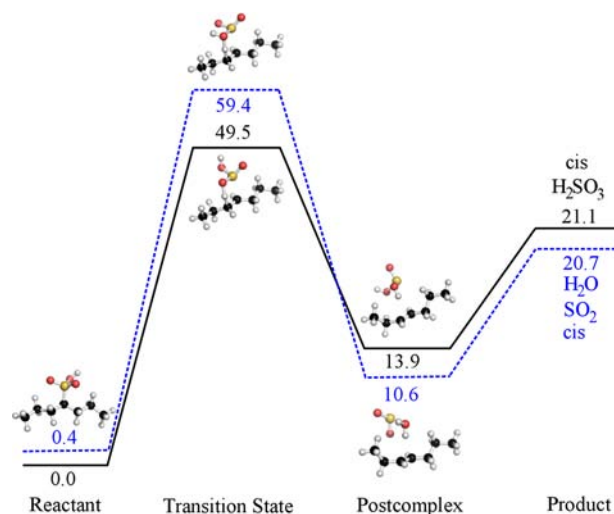


Figure 5. Representative reaction profiles for the E₅ reaction channels. Energy differences are in kcal/mol. Energies are zero-point corrected. See the Supporting Information for all channels and reaction profiles.

channels, R-SO₃H was positioned such that the S-OH was involved in the elimination (see dotted blue line in Figure 5). For these channels, elimination did not proceed to isolatable H₂SO₃, but upon stepping along the reaction coordinate from transition state to postcomplex, we found SO₂OH₂ undergoes a barrierless decomposition to give H₂O and SO₂. The barrier for these two channels was ~10 kcal/mol higher than that of the other channels. The bimolecular and trimolecular barriers for recombination were ~35 and 50 kcal/mol, respectively. Although it forms a relatively stable postcomplex, trimolecular recombination was not accounted for in the kMC simulations, as it was statistically unlikely to contribute to the overall pyrolysis reaction.

Following elimination, a postcomplex was formed that was 7–12 kcal/mol lower in energy than the infinitely separated products, where the lowest energy postcomplexes were formed through channels that gave H₂O and SO₂. All hept-3-ene products were the *cis* conformer. This fact will be used later in the kMC simulations to distinguish elimination products from the *trans*-olefin formed in the radical chain reaction.

α-H Abstraction by OH and HOSO₂ Radical. The radical chain reaction began with abstraction of one of four α-Hs by OH or HOSO₂. In the former case, the reaction proceeded

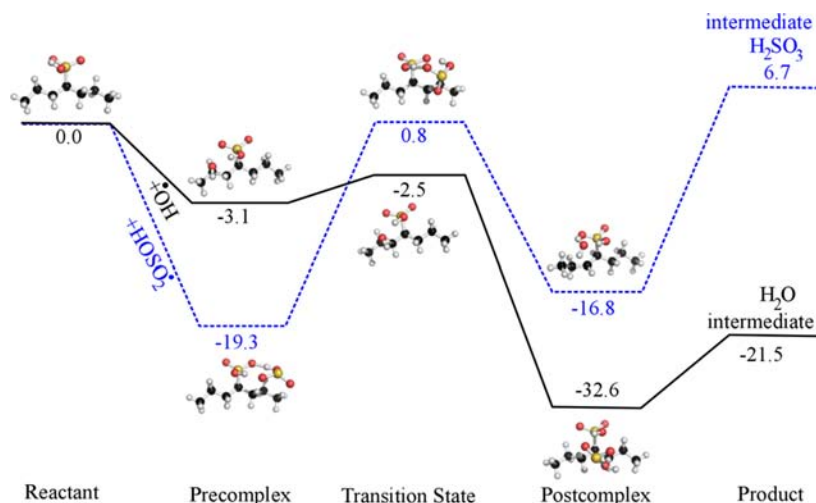


Figure 6. Representative reaction profiles for α -H abstraction by $\dot{\text{O}}\text{H}$ (black) and HOSO_2 (blue). Energy differences are in kcal/mol. Energies are zero-point corrected. See the Supporting Information for all channels and reaction profiles.

along 12 reaction channels. For the latter, 36 reaction channels were possible.

In regards to H abstraction by $\dot{\text{O}}\text{H}$, we observed reaction barriers of <5 kcal/mol for all reaction channels (Figure 6). In one-half of the precomplexes, we found that the H abstraction by $\dot{\text{O}}\text{H}$ radical was oriented so that it faced away from the sulfonic acid substituent (see the even-numbered channels in Supporting Information Figures S6 and S7). These precomplexes had no hydrogen bonding between the $\dot{\text{O}}\text{H}$ and the sulfonic acid, whereas the other channels did. Precomplexes with hydrogen bonding between the two reactants were stabilized by 1–4 kcal/mol relative to the infinitely separated reactants.

The reverse barrier for these channels (i.e., barriers for paths from products in postcomplex form to reactants' precomplex form) was 20–30 kcal/mol. The postcomplexes were 1–11 kcal/mol lower in energy than the infinitely separated products, where postcomplexes that featured hydrogen bonding between H_2O and the radical alkane intermediate were at a lower energy.

We successfully located 32 of the possible 36 transition states (see Computational Details) for α -H abstraction by HOSO_2 . Instead of forming a transition state, the remaining four reaction channels (see channels 5, 11, 23, and 29 in Supporting Information Figures S11, S13, and S15) had hydrogen bonding between HOSO_2 and H4S that disallowed positioning of reactants in close enough proximity for a transition state to form. All channels proceed through the formation of a precomplex that was 4–20 kcal/mol lower in the energy than the infinitely separated reactants, where the lowest-energy complexes had two hydrogen bonds between the reactants that formed an eight-centered ring (channels 4, 21, 22, 27, 31, and 35 in the Supporting Information). Two of the channels (22 and 27) had barriers of 20 kcal/mol, while the remaining barriers were higher. In these two channels, we found a transition state where two of the three oxygens from HOSO_2 were hydrogen bonding with the sulfonic acid in H4S (eight-centered ring). This interaction positioned the remaining oxygen to easily abstract the α -H and stabilized the transition state.

Postcomplexes were formed that were 4–12 kcal/mol lower in energy than the products (Figures S10, S12, and S14). The reaction was endothermic, with the final products at higher

energy than the reactants ($\Delta H = \sim 5$ kcal/mol). The reverse barrier varied from 10 to 30 kcal/mol across all channels. On the basis of all of the above information, we concluded that the rate-limiting step in the radical pyrolysis would be either α -H abstraction by HOSO_2 or HOSO_2 decomposition. The lowest barrier for α -H abstraction by HOSO_2 was 20 kcal/mol, and HOSO_2 decomposition had a barrier of 28 kcal/mol. In contrast, all other steps in the radical chain had much lower barriers.

Homolytic Cleavage of HOSO_2 from Radical Alkane Intermediate. After α -H abstraction, a radical alkane intermediate was formed. Homolytic cleavage of HOSO_2 from the radical alkane intermediate followed, with unimolecular barriers of 12–14 kcal/mol (see Figure 7 and

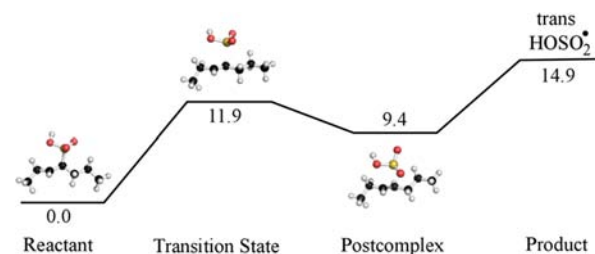


Figure 7. Representative reaction profile for the decomposition of the radical intermediate. Energy differences are in kcal/mol. Energies are zero-point corrected. See the Supporting Information for all channels and reaction profiles.

Supporting Information Figure S8). All forward reaction channels had similar energies and barriers, where we refer to the reaction profile for any one conformer as a reaction channel. The postcomplexes clustered around two energies. The majority (minority) were ~ 6 (9) kcal/mol lower in energy than the infinitely separated products. The reaction was endothermic, with the final products at higher energy than the radical intermediate. The four channels in the minority cluster (channels 0, 1, 6, and 7 in the Supporting Information) had a stabilizing interaction between H(O) from HOSO_2 and the double bond in hept-3-ene. Only two of the channels (3 and 7) resulted in *cis*-hept-3-ene; the remaining 10 gave the *trans* conformer. In the following section on pyrolysis

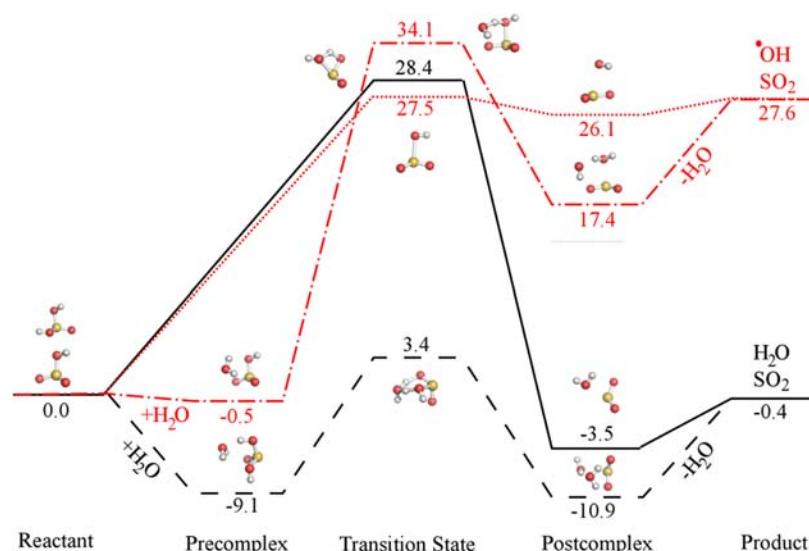


Figure 8. Reaction profiles for the unimolecular and H₂O-catalyzed decomposition of H₂SO₃ (black) and HOSO₂ (red) reaction channels. Energy differences are in kcal/mol. Energies are zero-point corrected.

Table 1. M06-2X/6-311++G(3df,3pd)//6-31G** Kooij Parameters from 300 to 1000 K for Various Reaction Steps^a

reaction	T (K)	ln B ^b	α	E ₀ ^c	k _i ' ^b (450 K)
E ₁ S Internal Elimination					
C ₇ H ₁₅ SO ₃ H → C ₇ H ₁₄ + H ₂ SO ₃ ^d	300–1000	33.40	0.00	50.08	1.378 × 10 ⁻¹⁰
C ₇ H ₁₄ + H ₂ SO ₃ → C ₇ H ₁₅ SO ₃ H	300–1000	-6.82	2.71	26.50	2.197 × 10 ⁻⁹
H ₂ SO ₃ Decomposition (Shared in Both Mechanisms)					
H ₂ SO ₃ → SO ₂ + H ₂ O	300–1000	29.36	0.00	27.79	1.738 × 10 ⁻¹
SO ₂ + H ₂ O → H ₂ SO ₃	300–1000	-3.65	2.68	25.60	1.220 × 10 ⁻⁷
H ₂ SO ₃ + H ₂ O → SO ₂ + 2H ₂ O	300–400	10.26	0.51	2.04	
	400–1000	-0.47	2.01	0.66	6.465 × 10 ⁴
Radical Chain Reaction					
C ₇ H ₁₅ SO ₃ H + $\dot{O}H$ → C ₇ H ₁₄ SO ₃ H + H ₂ O	300–800	-12.77	4.70	-6.96	1.988 × 10 ¹⁰
	800–1000	-4.77	3.65	-5.41	
C ₇ H ₁₄ SO ₃ H + H ₂ O → C ₇ H ₁₅ SO ₃ H + $\dot{O}H$	300–1000	-8.26	3.74	16.99	1.203 × 10 ⁻²
C ₇ H ₁₄ SO ₃ H → C ₇ H ₁₄ + HOSO ₂	300–1000	34.27	0.00	13.05	3.426 × 10 ⁸
C ₇ H ₁₄ + HOSO ₂ → C ₇ H ₁₄ SO ₃ H	300–600	-3.08	2.68	-3.17	2.074 × 10 ⁷
	600–1000	-2.45	2.59	-3.07	
C ₇ H ₁₅ SO ₃ H + HOSO ₂ → C ₇ H ₁₄ SO ₃ H + H ₂ SO ₃ ^d	300–550	-9.45	2.99	-2.86	1.615 × 10⁵
	550–1000	-61.06	9.98	-11.11	
C ₇ H ₁₄ SO ₃ H + H ₂ SO ₃ → C ₇ H ₁₅ SO ₃ H + HOSO ₂	300–700	-12.37	3.05	-8.76	9.751 × 10 ⁶
	700–1000	-69.27	10.69	-18.35	
HOSO ₂ → SO ₂ + $\dot{O}H$	300–1000	32.40	0.00	28.56	1.504 × 10 ⁰
SO ₂ + $\dot{O}H$ → HOSO ₂	300–400	9.42	1.42	-0.95	2.085 × 10 ⁸
	400–1000	3.96	2.19	-1.61	
HOSO ₂ + H ₂ O → SO ₂ + H ₂ O + $\dot{O}H$	300–1000	-3.76	2.72	31.09	3.014 × 10 ⁻¹⁰

^aRate data in black (italic) font increased (decreased) with temperature. Rates in bold had atypical behavior. ^bDepending on formation order, the rate constant k has units of s⁻¹ or M⁻¹ s⁻¹, where $k_i' = BT^\alpha e^{-E_0/RT}$. ^cE₀ has units of kcal/mol. ^dAlternatively SO₂OH₂, which decomposes to SO₂ + H₂O.

simulations, we will assign all radical chain products to *trans*-hept-3-ene. Because a *cis*-olefin was formed from the internal elimination, we will be able to ascertain which mechanism is active in the kMC simulations by separately following the two products.

H₂SO₃ and HOSO₂ Decomposition. The unimolecular and H₂O-catalyzed reaction profiles for the decomposition of H₂SO₃ and HOSO₂ are given in Figure 8. The H₂O-catalyzed decompositions began with the formation of a precomplex that was at a lower energy than the reactants. The barrier for unimolecular decomposition in both reactions was ~28 kcal/

mol. A minimum-energy postcomplex formed following decomposition of H₂SO₃ and HOSO₂, where the infinitely separated products were ~2–3 kcal/mol higher in energy than the postcomplex. A four-centered transition state was observed for the decomposition of H₂SO₃. H₂O-catalyzed decomposition of H₂SO₃ proceeded through a six-centered transition state with a barrier of 12.5 kcal/mol. Because H₂O was formed during the course of the pyrolysis simulation, H₂SO₃ decomposition proceeded predominantly via the bimolecular reaction.

The unimolecular decomposition of HOSO_2 advanced through a transition state where the HO-SO_2 bond elongated from 1.63 to 2.26 Å, with a barrier of 27.5 kcal/mol. H_2O -catalyzed decomposition of HOSO_2 progressed over a larger barrier (34.6 kcal/mol). The recombination of SO_2 and $\dot{\text{O}}\text{H}$ to give HOSO_2 had an activation barrier of only 1.4 kcal/mol. Only at higher temperatures does HOSO_2 decompose to $\dot{\text{O}}\text{H}$ and SO_2 . This was verified in the kMC simulations.

Cumulative Thermodynamic and Kinetic Data from All Reaction Channels. To report rate constants for temperatures from 300 to 1000 K, we fitted calculated rate constants to the Kooij equation (Table 1).^{36,53,54} The values reported are the sum over all reaction channels. We assumed that the rate constants for each conformer were additive (see kMC discussion later for verification). In many cases, two different curves were needed to accurately fit the data. For example, the recombination of $\text{SO}_2 + \dot{\text{O}}\text{H} \rightarrow \text{HOSO}_2$ was fit over the ranges 300–400 and 400–1000 K. Similarly, Somnitz also fit kinetic data for the recombination of hydroxylsulfonyl radical with multiple temperature ranges (see Supporting Information Figure S15 for a comparison with our work).⁴⁵

We also compared our rate constants for the formation of HOSO_2 and H_2SO_3 to those obtained from the literature (see Supporting Information Table S1). Our values were consistently smaller than those published for the formation of HOSO_2 and H_2SO_3 . The overall range of experimental and theoretical rate constants(s) at 300 K for formation of HOSO_2 , from literature was 8×10^8 to $2 \times 10^9 \text{ M}^{-1} \text{ s}^{-1}$.^{45,46,48,55} The literature value for H_2SO_3 formation was $4 \times 10^{-13} \text{ M}^{-1} \text{ s}^{-1}$.⁵⁶ Our respective values of 2×10^8 and $2 \times 10^{-14} \text{ M}^{-1} \text{ s}^{-1}$ for formation of HOSO_2 and H_2SO_3 were comparable. In the published reports, use of higher levels of theory for the theoretical rate constants (QCISD and CCSD(T)) and associated corrections decreased the reaction barriers, thereby increasing the rate constant.^{45,46,56} A difference in barrier of 1 kcal/mol at 300 K results in an order of magnitude change in the rate constant. Our barriers were higher than those reported, but by only ~ 1 kcal/mol.

Nonlinear Arrhenius behavior was observed for all bimolecular reactions. Cumulative rate constants were obtained from the expression $k_i' = k_i K_{\text{eq}}$ (see Computational Details). Excluding tunneling corrections, which were $1.1 \geq \kappa \geq 1.0$ from 300 to 1000 K, the unimolecular rate constant k_i had an exponential $1/T$ temperature dependence ($Ae^{-\Delta E/RT}$) and the expected negative slope in the Arrhenius plot. In contrast, the slope of $\ln(K_{\text{eq}})$ versus $1/T$ was positive because of the endothermic nature of the reaction. The opposing slopes introduced nonlinear behavior into the cumulative rate constant, and accounted for the concave curvature of the Arrhenius plot. This behavior is detailed in Figure 9A for $\text{C}_7\text{H}_{15}\text{SO}_3\text{H} + \text{HOSO}_2 \rightarrow \dot{\text{C}}_7\text{H}_{14}\text{SO}_3\text{H} + \text{H}_2\text{SO}_3$, where the natural log of the rate and equilibrium constants were both linear, but with opposite slopes. Therefore, the natural log of the cumulative rate constants was nonlinear.

To confirm that this behavior was not an artifact of the cumulative rate constant, which is the product of the equilibrium and rate constants ($k_i' = k_i K_{\text{eq}}$), we calculated rate constants for five bimolecular reaction channels from the infinitely separated reactants through the transition state (i.e., not going through a precomplex). These bimolecular values agreed with the cumulative rate constants to within four significant digits.

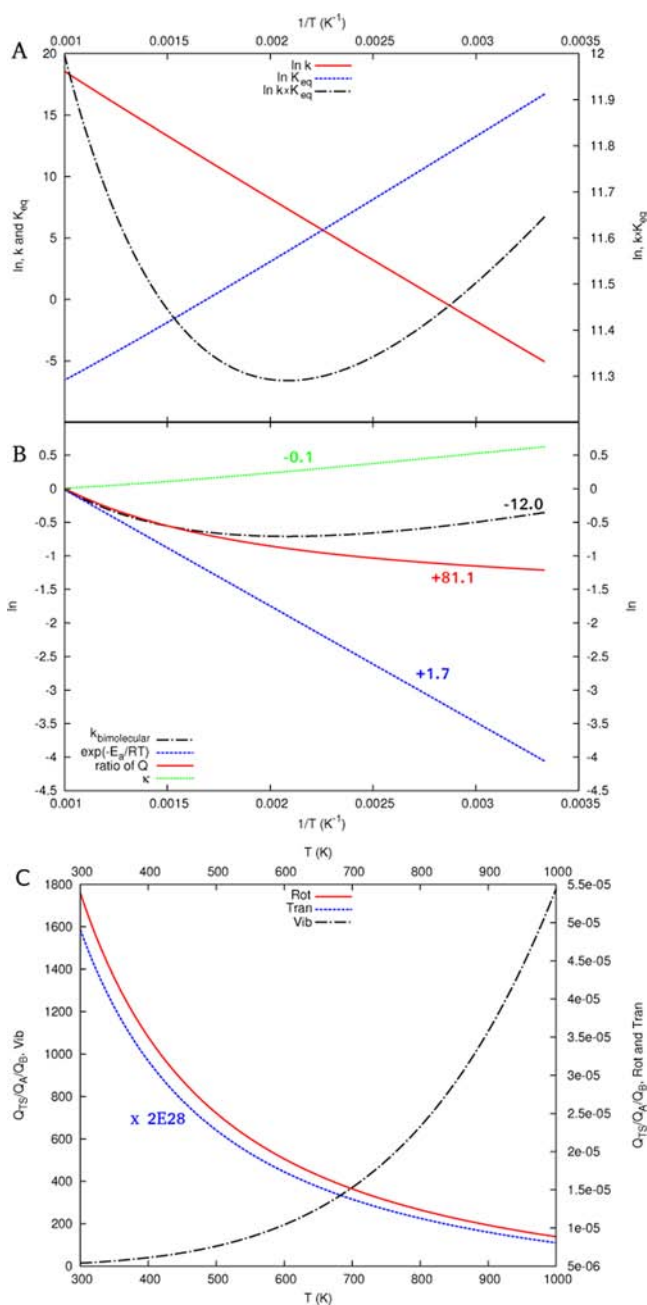


Figure 9. Plots for the reaction $\text{C}_7\text{H}_{15}\text{SO}_3\text{H} + \text{HOSO}_2 \rightarrow \dot{\text{C}}_7\text{H}_{14}\text{SO}_3\text{H} + \text{H}_2\text{SO}_3$ (channel 27). (A,B) Logarithmic plots versus $1/T$, unimolecular rate constant (k), equilibrium constant (K_{eq}), cumulative rate constant ($k \times K_{\text{eq}}$), bimolecular rate constant ($k_{\text{bimolecular}}$), energetic contribution (E_a), ratio of partition function (Q), and Wigner coefficient (κ). In (B), plots have been offset by the noted value. (C) Ratio of the partition functions versus T .

First, we analyzed the interplay between the activation energy and the ratio of the partition functions for bimolecular rate constants. We found that Arrhenius plots where the activation energy was small were nonlinear. For example, we observed in the recombination of $\text{SO}_2 + \dot{\text{O}}\text{H} \rightarrow \text{HOSO}_2$ that when the activation energy was greater than 10 kcal/mol (where we artificially altered the activation energy) the temperature dependence of the rate constants closely followed the exponential behavior (see Supporting Information Figure S17). However, if the activation energy was small, then the

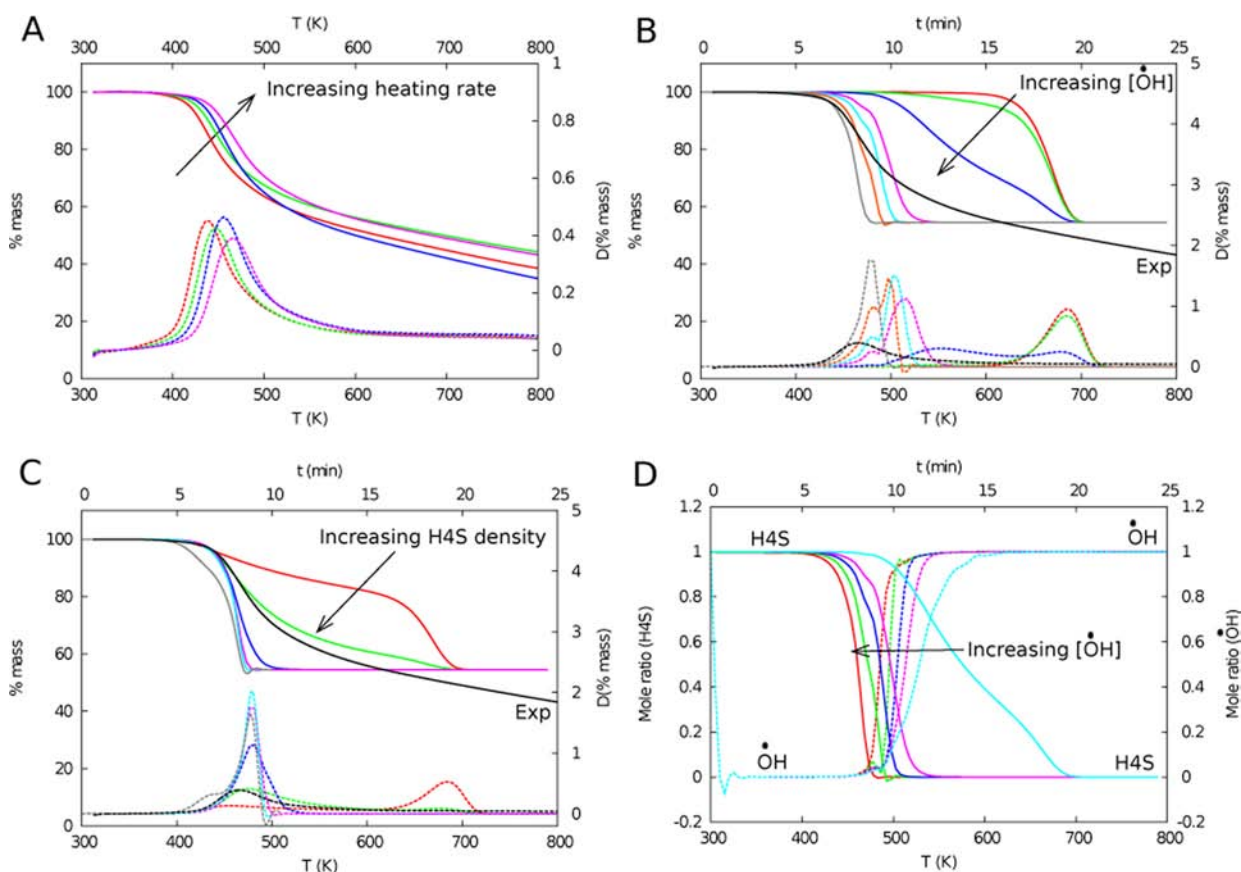


Figure 10. (A) Experimental TGAs based on sulfonated PE at heating rates of 2.5 (red), 5 (green), 10 (blue), and 20 (pink) °C/min. (B) H4S kMC simulations (1.6 ng mL⁻¹ 20 °C/min) detailing TGA dependence on $\dot{\text{O}}\text{H}/\text{H4S}$ ratio: 3.3×10^{-7} (red), 3.3×10^{-6} (green), 3.3×10^{-5} (blue), 3.3×10^{-4} (pink), 6.7×10^{-4} (aqua), 1.3×10^{-3} (orange), 2.7×10^{-3} (gray), and experimental (black, based on sulfonated PE). (C) H4S kMC simulations (20 °C/min) detailing TGA dependence on H4S density (first number) and high $\dot{\text{O}}\text{H}/\text{H4S}$ ratio (second number): 1.6 pg mL⁻¹, 6.7×10^{-3} (red); 16 pg mL⁻¹, 3.3×10^{-3} (green); 160 pg mL⁻¹, 2.7×10^{-3} (blue); 1.6 ng mL⁻¹, 2.7×10^{-3} (pink); 16 ng mL⁻¹, 2.7×10^{-3} (aqua); 160 ng mL⁻¹, 2.7×10^{-3} (gray); and experimental (black, based on sulfonated PE). (D) TGA (1.6 ng mL⁻¹ 20 °C/min) mole ratio of H4S and $\dot{\text{O}}\text{H}$ as a function of temperature/time with $\dot{\text{O}}\text{H}/\text{H4S}$ ratio: 3.3×10^{-5} (aqua), 3.3×10^{-4} (pink), 6.7×10^{-4} (blue), 1.3×10^{-3} (green), and 2.7×10^{-3} (red). See the Supporting Information for all TGAs.

temperature dependence of the entropic contribution became important, and nonlinear Arrhenius behavior was observed.

The reactions for which we observed nonlinear behavior (reactions with italic and bold-faced Kooij parameters in Table 1) had Kooij E_0 values < -2.86 kcal/mol. For example, in the reaction $\text{C}_7\text{H}_{15}\text{SO}_3\text{H} + \text{HOSO}_2 \rightarrow \dot{\text{C}}_7\text{H}_{14}\text{SO}_3\text{H} + \text{H}_2\text{SO}_3$ (channel 27), which had an activation barrier of 0.4 kcal/mol, we plotted the natural log of the bimolecular rate constant as a function of inverse temperature; see Figure 9B. We also included the individual contributions, that is, the exponential term and the ratio of partition functions, which comprise the entropic term. We observed that the ratio of the partition function decreased at a less than exponential rate with inverse temperature causing the deviation from Arrhenius behavior.

Furthermore, an analysis of the ratio of the rotational and translational partition functions ($(Q_{\text{TS}})/(Q_{\text{A}}Q_{\text{B}})$) showed that they varied little over the temperature range studied, but that the ratio of the vibrational partition function increased 2 or more orders of magnitude from 300 to 1000 K (see Figure 9C for example reaction $\text{C}_7\text{H}_{15}\text{SO}_3\text{H} + \text{HOSO}_2 \rightarrow \dot{\text{C}}_7\text{H}_{14}\text{SO}_3\text{H} + \text{H}_2\text{SO}_3$). To understand the strong temperature dependence of the ratio of the vibrational partition functions, we considered the change along the reaction path for the simple reaction $\dot{\text{O}}\text{H} + \text{SO}_2 \rightarrow \text{HOSO}_2$. Upon going from the infinitely separated

reactants to the transition state, six (five when $\dot{\text{O}}\text{H}$ was a reactant) rotational/translational modes in the reactants transitioned to vibrational modes (designated as transitional modes).⁵³ These modes did not cancel with corresponding modes in the vibrational partition functions of the reactants (with the exception of one mode due to the subtraction of the imaginary mode in the transition state). The remaining partition functions of the transitional modes increased polynomially with temperature (see Supporting Information Figures S18 and S19), which explains the temperature dependence observed in Figure 9B.

Theoretical and Experimental Thermogravimetric Analysis of Sulfonated PE. The pyrolysis of sulfonated PE was characterized by thermogravimetric analysis (TGA) at heating rates of 2.5, 5, 10, and 20 °C/min (see Figure 10A). The maximum mass loss occurred at 440–460 K.

We simulated the pyrolysis of H4S with kMC from 300 to 800 K using the calculated rate constants discussed earlier for internal elimination and the radical chain reaction mechanism. We are aware that other reactions occur at high temperatures, alkyl chain decomposition, but only the desulfonation was considered in this study. Examples of TGA plots are given in Figure 10 (see Supporting Information Figures S28–S35 for all kMC-simulated TGAs). Two assumptions were made during

the H4S kMC simulations. First, rate constants from all three conformers of H4S ([A], [B], and [C]) were summed to give an overall constant for each reaction step (as reported in Table 1). To validate this assumption, we compared TGA data generated by using the sum of the rate constants to one taking into consideration a Boltzmann distribution of the three conformers with their rate constants not being additive. We found an insignificant change.

Second, to distinguish between the contributions of the two mechanisms included in the simulations, we assigned all radical channels to the *trans*-olefin. Even though 2 of the 12 radical intermediate channels resulted in *cis*-hept-3-ene, the energy difference between the two isomers was only 0.1 kcal/mol. Conversely, we found that all products from internal elimination resulted in *cis*-hept-3-ene. By following separately the accumulation of *cis*- and *trans*-hept-3-ene, we were able to easily distinguish which mechanism was prevalent at any given temperature.

We initialized the radical mechanism by using trace amounts of $\dot{\text{O}}\text{H}$ and $\text{HOS}\dot{\text{O}}_2$. The simulated TGAs were identical (see Supporting Information Figure S37). The reason behind the identical TGAs will become apparent shortly. As such, we will only discuss those simulations that began with an initial amount of $\dot{\text{O}}\text{H}$.

From Figure 10B, we observed that the changes in H4S % mass at temperatures >600 K were independent of both H4S density and initial $\dot{\text{O}}\text{H}$ concentration. We concluded that first-order E_iS elimination became an important contributor to pyrolysis at these temperatures. This was independently verified by the presence of *cis*-hept-3-ene at temperatures >600 K (data not shown). For the remaining discussion, we will refer to the maximum change in % mass as a peak.

An $\dot{\text{O}}\text{H}$ radical concentration-dependent peak was observed at temperatures <550 K. Upon increasing the amount of initial $\dot{\text{O}}\text{H}$, this peak shifted to lower temperatures, eventually becoming independent of the initial $\dot{\text{O}}\text{H}$ concentration ($\dot{\text{O}}\text{H}/\text{H4S}$ ratio $\sim 10^{-3}$; see also Figure 10B). Depending on heating rate, at constant $\dot{\text{O}}\text{H}$ concentration, the peak varied from 440 to 480 K for all H4S densities (Figure 10C). This compared favorably to the peak observed experimentally from 440 to 460 K (Figure 10A) of sulfonated PE. The dominant products obtained at temperatures <550 K were *trans*-hept-3-ene, SO_2 , and H_2O (data not shown). The $\dot{\text{O}}\text{H}$ -dependent peak, and the accumulation of *trans*-hept-3-ene, were indicative of the radical mechanism.

Using the method of Flynn and Wall,²⁴ we calculated an experimental activation energy of ~ 31 kcal/mol for sulfonated PE (see Supporting Information Table S2). This compared favorably to the kMC activation energies at high concentrations of initial $\dot{\text{O}}\text{H}$ ($\dot{\text{O}}\text{H}/\text{H4S}$ ratio $\sim 10^{-3}$), 26–29 kcal/mol (see Supporting Information Figure S36). For low initial concentrations of $\dot{\text{O}}\text{H}$ ($\dot{\text{O}}\text{H}/\text{H4S}$ ratio $< 10^{-5}$), the kMC activation energies increased to 49–50 kcal/mol. This was consistent with the barrier for E_iS elimination.

To understand the $\dot{\text{O}}\text{H}$ -dependent behavior at temperatures <550 K, we analyzed the number of $\dot{\text{O}}\text{H}$, $\text{HOS}\dot{\text{O}}_2$, and radical intermediate molecules throughout the simulation. First, we observed that any initial $\dot{\text{O}}\text{H}$ reacted within the first few minutes of the simulation and that a steady-state concentration of $\text{HOS}\dot{\text{O}}_2$ accumulated at temperatures <450 K (data not shown). The same steady-state behavior was observed with those TGAs initialized with $\text{HOS}\dot{\text{O}}_2$. A sharp increase in $\text{HOS}\dot{\text{O}}_2$ decomposition was observed at temperatures ~ 450 K

(see Figure 10D). The peaks at 440–480 K corresponded to the onset of $\text{HOS}\dot{\text{O}}_2$ decomposition to $\dot{\text{O}}\text{H} + \text{SO}_2$. In this range, the conversion of H4S to product proceeded rapidly. Therefore, α -H abstraction by $\dot{\text{O}}\text{H}$ is the dominant path leading to product. There was no accumulation of the radical intermediate (data not shown). This means that following α -H abstraction, $\text{HOS}\dot{\text{O}}_2$ dissociated rapidly from the radical alkane intermediate to give product and $\text{HOS}\dot{\text{O}}_2$. We concluded that the rate-limiting step of the radical chain mechanism was the decomposition of $\text{HOS}\dot{\text{O}}_2$ to $\dot{\text{O}}\text{H} + \text{SO}_2$. This is supported by the fact that the activation energy derived from the TGA is consistent with the barrier for $\text{HOS}\dot{\text{O}}_2$ decomposition.

CONCLUSIONS

To understand pyrolysis pathways of sulfonated PE, we have studied the decomposition reactions of the model compound H4S. Using density functional theory and transition state theory, we have determined the rate constants for the internal elimination (E_iS) and radical chain reaction mechanism for the pyrolysis of H4S.

Nonlinear Arrhenius plots were found for all bimolecular reactions. To report and interpret rate constants, we used the Kooij equation. For reactions with low activation barriers, nonlinearity was traced to conflicting trends between the exponential temperature dependence of the energetic term and the vibrational partition function of the transitional modes. For reactions with high activation energies, the exponential term was dominant, and the Arrhenius plot approached linearity.

This work represents the first study of E_iS elimination in alkane sulfonic acid derivatives. Two different reaction barriers were found (50 and 60 kcal/mol), depending on the placement of the HO-group in the sulfonic acid. $\text{R}-\text{CHSO}_3\text{H}$ rotation from the reactant to the transition state yielded a *cis*-alkene. The decomposition of the product, H_2SO_3 , was aided catalytically by H_2O , with a barrier of 16 kcal/mol.

Following radical abstraction of the α -H from H4S, first-order decomposition of the radical intermediate yielded the *trans*-alkene and $\text{HOS}\dot{\text{O}}_2$. At temperatures <440 K, the amount of H4S converted to the olefin was insignificant. At higher temperatures, $\text{HOS}\dot{\text{O}}_2$ underwent decomposition to $\dot{\text{O}}\text{H} + \text{SO}_2$, which allowed for rapid α -H abstraction by $\dot{\text{O}}\text{H}$. Given the reported BDEs for the resulting olefin, we predict that the increasing presence of unsaturated bonds during the course of pyrolysis will augment the amount of $\dot{\text{O}}\text{H}$, and will therefore increase the available amount of free radical to initiate the radical chain.

We have used kMC, in conjunction with DFT/TST-determined rate constants, to simulate TGAs, which were used experimentally to follow pyrolysis. We found two regions in the TGA that were dominated by different mechanisms. At temperatures >600 K, a concerted unimolecular reaction was present that produced a *cis*-alkene. At temperatures from 440 to 550 K, a radical reaction produced a *trans*-alkene. In this region, the maximum rates of change in % mass occurred from 440 to 480 K, depending on heating rate. At these temperatures, $\text{HOS}\dot{\text{O}}_2$ decomposed and $\dot{\text{O}}\text{H}$ became the radical responsible for propagation of the chain reactions. The maximum rates of change in the radical region of the TGA agree with what is observed experimentally (440–460 K). Low-scale pyrolysis of sulfonated PE utilizes temperatures <620 K, making the radical mechanism the dominant pathway in the production of carbonaceous unsaturated hydrocarbon that, subsequently,

undergoes carbonization at very high temperature. Such carbonization studies will be conducted in future investigations.

■ ASSOCIATED CONTENT

● Supporting Information

Convergence criteria for geometry optimizations. Table of HOSO₂ and H₂SO₃ rate constants. Table of experimental activation energies. TEM of fully sulfonated precursor. Reaction profiles and channels. Plot of rate constant comparison for SO₂ + OH → HOSÖ₂ (this work) and previous results from Somnitz.⁴⁵ Plots of unimolecular, equilibrium, and cumulative bimolecular rate constants. Activation energy dependence of the Arrhenius plot and transitional modes for OH + SO₂ → HOSÖ₂. Plots of bimolecular partition functions. TGA plots and activation energies. Cartesian coordinates and energies of calculated structures (and displacement energies if necessary). This material is available free of charge via the Internet at <http://pubs.acs.org>.

■ AUTHOR INFORMATION

Corresponding Author

younkerjm@ornl.gov

Notes

The authors declare no competing financial interest.

■ ACKNOWLEDGMENTS

We would like to acknowledge Marv Potsma and A. C. Buchanan, III at ORNL for their help and expertise. We would also like to acknowledge Joshua H. Perkins and Tyler A. Tommey at ORNL for their support. This work was sponsored by the Office of Advanced Scientific Computing Research, U.S. Department of Energy, and was performed in part using the resources of the National Center for Computational Sciences at Oak Ridge National Laboratory under contract DE-AC05-00OR22725 and the National Institute for Computational Sciences provided by the National Science Foundation.

■ REFERENCES

- (1) Chung, D. D. L. *Carbon Fiber Composites*; Elsevier: New York, 1994.
- (2) Frank, E.; Hermantuz, F.; Buchmeiser, M. R. *Macromol. Mater. Eng.* **2012**, *297*, 493–501.
- (3) Nataraj, S. K.; Yang, K. S.; Aminabhavi, T. M. *Prog. Polym. Sci.* **2012**, *37*, 487–513.
- (4) Warren, C. D.; Paulauskas, F. L.; Baker, F. S.; Eberle, C. C.; Naskar, A. *SAMPE J.* **2009**, *45*, 24–36.
- (5) Peacock, A. J. *Handbook of Polyethylene: Structures, Properties, and Applications*; CRC Press: New York, 2000.
- (6) Postema, A. R.; De Groot, H.; Pennings, A. J. *J. Mater. Sci.* **1990**, *25*, 4216–4222.
- (7) McCaffrey, W. C.; Kamal, M. R.; Cooper, D. G. *Polym. Degrad. Stab.* **1995**, *47*, 133–139.
- (8) Lawson, J. W.; Srivastava, D. *Phys. Rev. B* **2008**, *77*, 114209.
- (9) Hunt, M. A.; Saito, T.; Brown, R. H.; Kumbhar, A. S.; Naskar, A. K. *Adv. Mater.* **2012**, *24*, 2386–2389.
- (10) Stapersma, J.; Deuling, H. H.; van Ginkel, R. *J. Am. Oil Chem. Soc.* **1992**, *69*, 39–43.
- (11) Choi, Y. B.; Park, O. O. *J. Appl. Polym. Sci.* **2008**, *109*, 736–748.
- (12) Kaneko, M.; Kumagai, S.; Nakamura, T.; Sato, H. *J. Appl. Polym. Sci.* **2004**, *91*, 2435–2442.
- (13) Wang, H.; Chen, S.; Zhang, J. *Colloid Polym. Sci.* **2009**, *287*, 541–548.
- (14) Smith, M. B.; March, J. *March's Advanced Organic Chemistry*, 5th ed.; John Wiley & Sons: New York, 2001; pp 1298–1376.
- (15) Cubbage, J. W.; Vos, B. W.; Jenks, W. S. *J. Am. Chem. Soc.* **2000**, *122*, 4968–4971.
- (16) Cubbage, J. W.; Guo, Y.; McCulla, R. D.; Jenks, W. S. *J. Org. Chem.* **2001**, *66*, 8722–8736.
- (17) Claes, L.; François, J.-P.; Deleuze, M. S. *J. Am. Chem. Soc.* **2002**, *124*, 7563–7572.
- (18) Claes, L.; François, J.-P.; Deleuze, M. S. *J. Am. Chem. Soc.* **2003**, *125*, 7129–7138.
- (19) Zhao, Y.-L.; Jones, W. H.; Monnat, F.; Wudl, F.; Houk, K. N. *Macromolecules* **2005**, *38*, 10279–10285.
- (20) Kingsbury, C. A. *J. Phys. Org. Chem.* **2010**, *23*, 513–518.
- (21) McCulla, R. D.; Cubbage, J. W.; Jenks, W. S. *J. Phys. Org. Chem.* **2002**, *15*, 71–77.
- (22) Werkema, E. L.; Castro, L.; Maron, L.; Eisenstein, O.; Anderson, R. A. *Organometallics* **2012**, *31*, 870–881.
- (23) Mansfield, E.; Kar, A.; Quinn, T. P.; Hooker, S. A. *Anal. Chem.* **2010**, *82*, 9977–9982.
- (24) Flynn, J. H.; Wall, L. A. *Polym. Lett* **1966**, *5*, 323–328.
- (25) Bylaska, E. J.; et al. *NWChem, A Computational Chemistry Package for Parallel Computers, Version 6.0*; Pacific Northwest National Laboratory: Richland, WA, 2010.
- (26) Zhao, Y.; Truhlar, D. G. *Theor. Chem. Acc.* **2008**, *120*, 215–241.
- (27) Zhao, Y.; Schultz, N. E.; Truhlar, D. G. *J. Chem. Theory Comput.* **2006**, *2*, 364–382.
- (28) Denis, P. A. *J. Chem. Theory Comput.* **2005**, *1*, 900–907.
- (29) Korang, J.; Grither, W. R.; McCulla, R. D. *J. Phys. Chem. A* **2011**, *115*, 2859–2865.
- (30) Stoffregen, S. A.; McCulla, R. D.; Wilson, R.; Cercone, S.; Miller, J.; Jenks, W. S. *J. Org. Chem.* **2007**, *72*, 8235–8242.
- (31) McCulla, R. D.; Jenks, W. S. *J. Org. Chem.* **2003**, *68*, 7871–7879.
- (32) Wheeler, S. E.; Houk, K. N. *J. Chem. Theory Comput.* **2010**, *6*, 395–404.
- (33) Holbrook, K. A.; Piling, M. J.; Robertson, S. H. *Unimolecular Reactions*, 2nd ed.; John Wiley & Sons: Chichester, England, 1996.
- (34) Henriksen, N. E.; Hansen, F. Y. *Theories of Molecular Reaction Dynamics: The Microscopic Foundation of Chemical Kinetics*; Oxford University Press: New York, 2008.
- (35) Beste, A.; Buchanan, A. C., III; Britt, P. F.; Hathorn, B. C.; Harrison, R. J. *J. Phys. Chem. A* **2007**, *111*, 12118–12126.
- (36) Kooij, D. M. *Z. Phys. Chem.* **1893**, *12*, 155.
- (37) Plimpton, S.; Battaile, C.; Chandross, M.; Holm, L.; Thompson, A.; Tikare, V.; Wagner, G.; Webb, E.; Zhou, X.; Cardona, C. G.; Slepoy, A. *Crossing the Mesoscale No-Man's Land via Parallel Kinetic Monte Carlo*; SANDIA, 2009.
- (38) *Core Research Development Team, R: A Language and Environment for Statistical Computing*; R Foundation for Statistical Computing: Vienna, Austria, 2008.
- (39) Luo, Y.-R., Ed. *Handbook of Bond Dissociation Energies in Organic Compounds*; CRC Press: London, 2003.
- (40) Ma, S.; Lu, J.; Gao, J. *Energy Fuels* **2002**, *16*, 338–342.
- (41) Wang, Y.; Wang, X.; Liu, L.; Peng, X. *J. Mol. Struct. (THEOCHEM)* **2009**, *896*, 34–37.
- (42) Emerson, D. W.; Craig, A. P.; Potts, I. W., Jr. *J. Org. Chem.* **1967**, *32*, 102–104.
- (43) Wai-Kee, L.; McKee, M. L. *J. Phys. Chem. A* **1997**, *101*, 9778–9782.
- (44) Moore-Plummer, P. L.; Wu, R.; Flenner, J. *J. Mol. Phys.* **2002**, *100*, 1847–1853.
- (45) Somnitz, H. *Phys. Chem. Chem. Phys.* **2004**, *6*, 3844–3851.
- (46) Sitha, S.; Jewell, L. L.; Piketh, S. J.; Fourie, G. *Atmos. Environ.* **2011**, *45*, 745–754.
- (47) Atkinson, R.; Baulch, D. L.; Cox, R. A.; Hampson, R. F.; Kerr, J. A.; Rossi, M. J.; Troe, J. *J. Phys. Chem. Ref. Data* **1997**, *26*, 521–1101.
- (48) Blitz, M. A.; Hughes, K. J.; Pilling, M. J. *J. Phys. Chem. A* **2003**, *107*, 1971–1978.
- (49) Sülzle, D.; Verhoeven, M.; Terlou, J. K.; Schwarz, H. *Angew. Chem., Int. Ed. Engl.* **1988**, *27*, 1533–1534.
- (50) Voegelé, A. F.; Tautermann, C. S.; Loerting, T.; Hallbrucker, A.; Mayer, E.; Liedl, K. R. *Chem.-Eur. J.* **2002**, *8*, 5644–5651.

- (51) Steudel, R.; Steudel, Y. J. *Phys. Chem. A* **2009**, *113*, 9920–9933.
- (52) Li, P.; Ma, Z.-Y.; Wang, W.-H.; Shen, Z.-T.; Bi, S.-W.; Sun, H.-T.; Bu, Y.-X. *ChemPhysChem* **2010**, *11*, 696–705.
- (53) Masgrau, L.; Gonzalez-Lafont, A.; Lluch, J. M. *Theor. Chem. Acc.* **2003**, *110*, 352–357.
- (54) Galano, A.; Alvarez-Idaboy, J. R.; Francisco-Marquez, M. J. *Phys. Chem. A* **2010**, *114*, 7525–7536.
- (55) Fulle, D.; Hamann, H. F.; Hippler, H. *Phys. Chem. Chem. Phys.* **1999**, *1*, 2695–2702.
- (56) Vahedpour, M.; Zolfaghari, F. *Struct. Chem.* **2011**, *22*, 1331–1338.